INSTITUTE OF PHYSICS PUBLISHING COMBUSTION THEORY AND MODELLING

Combust. Theory Modelling **6** (2002) 173–187 PII: S1364-7830(02)28192-9

The flame preheating effect on numerical modelling of soot formation in a two-dimensional laminar ethylene–air diffusion flame

Hongsheng Guo[1,3], **Fengshan Liu**[1], **Gregory J Smallwood**[1] **and Ömer L Gülder**[2]

[1] Combustion Research Group, Building M-9, Institute for Chemical Process and Environmental Technology, National Research Council of Canada, 1200 Montreal Road, Ottawa, Ontario, Canada K1A 0R6
[2] Institute for Aerospace Studies, University of Toronto, 4925 Dufferin Street, Toronto, Ontario, Canada M3H 5T6

E-mail: hongsheng.guo@nrc.ca

Received 22 August 2001, in final form 21 January 2002
Published 18 March 2002
Online at stacks.iop.org/CTM/6/173

Abstract

Numerical modelling of soot formation is conducted for an axisymmetric, laminar, coflow diffusion ethylene–air flame by two different methods to investigate the effect of flame preheating. The first method cannot account for the preheating effect, while the second one can. A detailed gas-phase reaction mechanism and complex thermal and transport properties are used. The fully coupled elliptic equations are solved. A simple two-equation soot model is used to model the soot process coupled with detailed gas-phase chemistry. The numerical results are compared with experimental data and indicate that the flame preheating effect has a significant influence on the prediction of soot yields. Both methods give reasonable flame temperature and soot volume fraction distributions. However, quantitatively the second method results in improved flame temperatures and soot volume fractions, especially in the region near the fuel inlet, although the maximum flame temperatures from both methods are slightly lower than that from the experiment.

1. Introduction

Soot is a by-product of incomplete hydrocarbon combustion. The detrimental effect of soot on human health is a current concern and various restrictions are being placed on soot emissions from various sources. From an operational point of view, soot formation is not desired in most combustion devices. Therefore, a quantitative understanding of soot inception, growth and

[3] Author to whom correspondence should be addressed.

oxidation mechanisms and the ability to model these processes are critical to the development of strategies to control soot emissions.

Two-dimensional axisymmetric, laminar diffusion flames are the typical flames that have been widely used to investigate soot formation and other flame characteristics. Numerous experiments have been conducted in the last century and several numerical studies have appeared in the past decade for these flames. An important step to exactly model this kind of flame is the specification of appropriate boundary conditions. Unfortunately, it is usually difficult to know the exact inlet temperature and velocity profiles due to the flame preheating caused by heat transfer from the flame base to the burner nozzle and both fuel and air streams. This preheating effect was, in general, neglected and instead uniform inlet temperature and velocity were specified by most investigators [1–4]. In the modelling of soot formation in a coflow, laminar diffusion flame, Smooke *et al* [5] raised both fuel and air inlet temperatures by 120 K, since they found that the flame temperatures were underpredicted by about 100–150 K when the preheating was not accounted for. In order to minimize the uncertainty of inlet conditions, McEnally *et al* [6] modelled a lifted flame by specifying the room temperature as inlet temperatures for both air and fuel streams, and a parabolic velocity profile for the fuel stream and a uniform velocity distribution for the air stream. However, most experiments were conducted for burner stabilized flames. In the modelling of soot formation of a coflow, laminar ethylene–air diffusion flame [7], we found that the temperatures in the lower centreline region were significantly underpredicted, even though we increased both the fuel and air inlet temperatures by 40 K to account for the flame preheating and a parabolic velocity profile was specified for the fuel stream.

Apparently, difficulties exist for specifying an appropriate inlet boundary condition for the simulation of this kind of flame. Although the prediction results can be improved by raising both fuel and air inlet temperatures to a certain extent, it is usually hard to know the exact value by which it is to be raised. Moreover, the extents of preheating of fuel and air streams may be different due to different flow rates, and thus their inlet temperatures are generally different. Thirdly, the inlet velocity profiles of both the fuel and air streams may be neither the general shapes of fully developed laminar flows in a round pipe and a concentric space nor uniform distributions, due to the preheating.

In this paper, we numerically model a two-dimensional axisymmetric laminar ethylene–air diffusion flame by two different methods of dealing with the inlet conditions to identify the effect of flame preheating on the numerical results, especially on the soot formation process. The first method employed is similar to those used by most previous investigators, and thus cannot accurately account for the influence of preheating. In the second method, we extend the simulation domain into the fuel nozzle a certain distance, and therefore the flame preheating effect can be accounted for by simulation itself. Computationally, we employ the primitive variable method in which the fully elliptic governing equations are solved with detailed gas-phase chemistry and complex thermal and transport properties. A simplified soot model is used to simulate soot formation in the flame. The effects of soot inception, growth and oxidation on gas-phase chemistry are taken into account. The radiation heat loss is accounted for by the discrete ordinate method coupled to an SNBCK-based wide-band model for radiative properties of CO, CO_2, H_2O and soot. The results are compared to those obtained in our laboratory by Gülder *et al* [8].

2. Numerical methods

2.1. Flame configuration

The investigated flame is a coflow, laminar ethylene–air diffusion flame in which a cylindrical fuel (ethylene) stream is surrounded by a coflowing air jet.

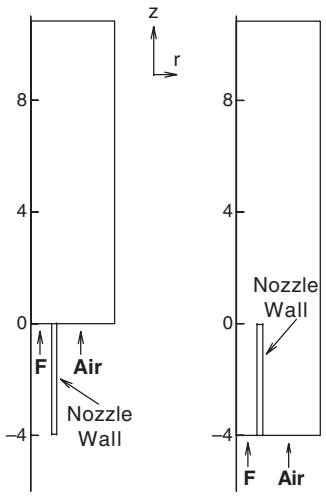

Figure 1. Burner configuration. Left: domain of simulation 1; right: domain of simulation 2.

We use two methods of dealing with the inlet conditions to simulate this flame. In the simulation by the first method (simulation 1), the computational domain covers an area from 0 to 3.0 cm in the radial direction and from 0 to 11.0 cm in the axial direction. It has been checked by a sensitivity calculation that this computational domain is enough and thus the boundary location does not influence the simulation results. The inflow boundary ($z = 0$) corresponds to the region immediately above the fuel nozzle exit. A uniform velocity of 3.54 cm s^{-1} is used for the region from $r = 0$ to 0.545 cm (fuel nozzle exit) at $z = 0$, and that of 62.52 cm s^{-1} is used for the region from $r = 0.64$ to 3.0 cm (air nozzle exit) at $z = 0$. The inlet temperatures of both fuel and air streams are 300 K. For the region from $r = 0.545$ to 0.64 cm at $z = 0$, a solid wall boundary condition is used. Symmetric and free-slip boundary conditions are used for $r = 0$ and $r = 3.0$ cm, respectively. At z= 11.0 cm, a zero-gradient outlet boundary condition is employed.

In the second simulation (simulation 2), the above computational domain is extended into the fuel nozzle a certain distance where the nozzle wall temperature approximately reaches room temperature, so that part of the fuel nozzle is included in the simulation domain. This extended distance is 4 cm in the present simulation. The boundary conditions are the same as those in simulation 1, except that the inlet of the domain is moved to $z = -4$ cm. By specifying a linear temperature distribution (with values of 300 and 403 K at $z = -4$ and 0 cm, respectively) along the axis direction for the solid wall of the fuel nozzle according to the experimental measurements of Gülder *et al* [9], the conduction and convection heat transfer from the wall of the fuel nozzle and flame base to both fuel and air streams is taken into account. The radiation heat transfer from the nozzle wall is neglected, since the wall temperature is very low (400 K).

Figure 1 shows the burner configuration and calculation domains for the two simulations.

2.2. Gas-phase equations

In cylindrical coordinates (r, z), the governing equations for the gas phase are [10] as follows.

Continuity:

$$\frac{\partial}{\partial r}(r\rho v) + \frac{\partial}{\partial z}(r\rho u) = 0. \tag{1}$$

Axial momentum:

$$\rho v\frac{\partial u}{\partial r}+\rho u\frac{\partial u}{\partial z}=-\frac{\partial p}{\partial z}+\frac{1}{r}\frac{\partial}{\partial r}\left(r\mu\frac{\partial u}{\partial r}\right)+2\frac{\partial}{\partial z}\left(\mu\frac{\partial u}{\partial z}\right)-\frac{2}{3}\frac{\partial}{\partial z}\left(\frac{\mu}{r}\frac{\partial}{\partial r}(rv)\right)$$
$$-\frac{2}{3}\frac{\partial}{\partial z}\left(\mu\frac{\partial u}{\partial z}\right)+\frac{1}{r}\frac{\partial}{\partial r}\left(r\mu\frac{\partial v}{\partial z}\right)+\rho g_z. \tag{2}$$

Radial momentum:

$$\rho v\frac{\partial v}{\partial r}+\rho u\frac{\partial v}{\partial z}=-\frac{\partial p}{\partial r}+\frac{\partial}{\partial z}\left(\mu\frac{\partial v}{\partial z}\right)+\frac{2}{r}\frac{\partial}{\partial r}\left(r\mu\frac{\partial v}{\partial r}\right)-\frac{2}{3}\frac{1}{r}\frac{\partial}{\partial r}\left(\mu\frac{\partial}{\partial r}(rv)\right)$$
$$-\frac{2}{3}\frac{1}{r}\frac{\partial}{\partial r}\left(r\mu\frac{\partial u}{\partial z}\right)+\frac{\partial}{\partial z}\left(\mu\frac{\partial u}{\partial r}\right)-\frac{2\mu v}{r^2}+\frac{2}{3}\frac{\mu}{r^2}\frac{\partial}{\partial r}(rv)+\frac{2}{3}\frac{\mu}{r}\frac{\partial u}{\partial z}. \tag{3}$$

Energy:

$$c_p\left(\rho v\frac{\partial T}{\partial r}+\rho u\frac{\partial T}{\partial z}\right)=\frac{1}{r}\frac{\partial}{\partial r}\left(r\lambda\frac{\partial T}{\partial r}\right)+\frac{\partial}{\partial z}\left(\lambda\frac{\partial T}{\partial z}\right)$$
$$-\sum_{k=1}^{KK+1}\left[\rho c_{pk}Y_k\left(V_{kr}\frac{\partial T}{\partial r}+V_{kz}\frac{\partial T}{\partial z}\right)\right]-\sum_{k=1}^{KK+1}h_kW_k\omega_k+q_r. \tag{4}$$

Gas species:

$$\rho v\frac{\partial Y_k}{\partial r}+\rho u\frac{\partial Y_k}{\partial z}=-\frac{1}{r}\frac{\partial}{\partial r}(r\rho Y_kV_{kr})-\frac{\partial}{\partial z}(\rho Y_kV_{kz})+W_k\omega_k,\qquad k=1,2,\ldots,KK. \tag{5}$$

u and v are the velocities in the axial (z) and radial (r) directions, respectively, T the temperature of the mixture, ρ the density of the mixture (soot and gas), W_k the molecular weight of the kth gas species, λ the mixture thermal conductivity, c_p the specific heat of the mixture under constant pressure, c_{pk} the specific heat of the kth gas species under constant pressure and ω_k the mole production rate of the kth gas species per unit volume. It should be pointed out that the production rates of gas species include the contribution due to soot inception, surface growth and oxidation (see the next section). Quantity h_k denotes the specific enthalpy of the kth gas species, g_z the gravitational acceleration in the z direction, μ the viscosity of the mixture, Y_k the mass fraction of the kth gas species, V_{kr} and V_{kz} the diffusion velocities of the kth gas species in the r and z directions and KK the total gas-phase species number. The quantities with subscript $KK+1$ correspond to those of soot. As an approximation, the thermal properties, obtained from JANAF thermochemical tables [11], of graphite are used to represent those of soot.

The last term on the right-hand side of equation (4) is the source term due to radiation heat transfer. It is obtained by the discrete ordinate method coupled to an SNBCK-based wide-band model for properties of CO, CO_2, H_2O and soot. The model is formulated by lumping successive 20 narrow-bands (bandwidth $25\,cm^{-1}$) to form a wide-band of $500\,cm^{-1}$, based on the band-lumping strategy described in [12]. A total of 20 wide-bands are considered in the calculation to cover the infrared spectrum between 150 and $9100\,cm^{-1}$. At each wide-band, the blackbody radiation intensity and the absorption coefficient of soot are calculated at the band centre. The absorption coefficients of the gas mixture containing CO, CO_2 and H_2O at the Gauss quadrature points within each wide-band are obtained using the method similar to the SNBCK technique in [13]. The approximate Malkmus band method based on the expressions in the optically thin limit described by Liu *et al* [14] is used to treat the gas mixture as a single radiating gas. The two-point Gauss quadrature is employed in the present calculations to reduce the computing time while maintaining accuracy based on the findings in [15]. The model parameters of the statistical narrow-band model for CO, CO_2 and H_2O are

those compiled recently by Soufiani and Taine [16] based on line-by-line calculations. The spectral absorption coefficient of soot is obtained by Rayleigh's theory for small particles and the refractive index of soot due to Dalzell and Sarofim [17], and it turns out to be about $5.5 f_v/\lambda$ (where f_v is the soot volume fraction and λ the wavelength).

The diffusion velocity is written as

$$V_{kx_i} = -\frac{1}{Y_k} D_k \frac{\partial Y_k}{\partial x_i} + V_{Tkx_i} + V_{cx_i}, \qquad k = 1, 2, \ldots, KK, \tag{6}$$

where V_{Tkx_i} is the thermal diffusion velocity in the x_i direction for the kth gas species and V_{cx_i} is the correction diffusion velocity used to ensure that the net diffusive flux of all gas species and soot is zero [18] in the x_i direction. In the current simulation, only the thermal diffusion velocities of the H_2 and H species are accounted for by [18]

$$V_{Tkx_i} = \frac{D_k \Theta_k}{X_k} \frac{1}{T} \frac{\partial T}{\partial x_i}, \tag{7}$$

while those of all other gas species are set as zero. Quantity D_k is related to the binary diffusion coefficients through the relation

$$D_k = \frac{1 - X_k}{\sum_{j \neq k}^{KK} X_j / D_{jk}}, \qquad k = 1, 2, \ldots, KK, \tag{8}$$

where Θ_k is the thermal diffusion ratio of the kth species, X_k is the mole fraction of the kth species and D_{jk} is the binary diffusion coefficient.

2.3. Soot model

Modelling soot formation in practical combustion systems is an extremely challenging problem. Although some detailed kinetic models of soot inception, growth and oxidation have been derived, such as those in [19–21], it is currently still very difficult and time consuming to implement this kind of model to the simulations of multidimensional combustion systems. The applicability of purely empirical soot models is questionable under conditions different from those under which they were originally formulated. Based on some semi-empirical assumptions, Smooke *et al* [5] and McEnally *et al* [6] used the sectional model to simulate the soot formation process. In addition to the momentum, energy and gas species conservation equations, several soot section equations (usually more than ten) need to be solved. Leung *et al* [22] and Fairweather *et al* [23] also conducted simulations of soot formation by a simplified two-equation soot model based on similar semi-empirical assumptions. Except those of gas-phase governing equations, only two additional equations need to be solved for the soot process in this model. Therefore, it is used in this paper.

Two transport equations are solved for soot mass fraction and number density, respectively. They are

$$\rho v \frac{\partial Y_s}{\partial r} + \rho u \frac{\partial Y_s}{\partial z} = -\frac{1}{r} \frac{\partial}{\partial r}(r \rho V_{T,r} Y_s) - \frac{\partial}{\partial z}(\rho V_{T,z} Y_s) + S_m, \tag{9}$$

$$\rho v \frac{\partial N}{\partial r} + \rho u \frac{\partial N}{\partial z} = -\frac{1}{r} \frac{\partial}{\partial r}(r \rho V_{T,r} N) - \frac{\partial}{\partial z}(\rho V_{T,z} N) + S_N, \tag{10}$$

where Y_s is the soot mass fraction and N is the soot number density defined as the particle number per unit mass of mixture. Quantities $V_{T,r}$ and $V_{T,z}$ are the particle thermophoretic velocities in the r and z directions, respectively. They are obtained by [24]

$$V_{T,x_i} = -0.55 \frac{\mu}{\rho T} \frac{\partial T}{\partial x_i}, \qquad x_i = r, z. \tag{11}$$

The source term S_m in equation (9) accounts for the contributions of soot nucleation (ω_n), surface growth (ω_g) and oxidation (ω_O). Therefore,

$$S_m = \omega_n + \omega_g - \omega_O. \tag{12}$$

The model developed by Leung *et al* [22] and Fairweather *et al* [23] is used to obtain the three terms on the right-hand side of equation (12). It assumes the chemical reactions for nucleation and surface growth, respectively, as

$$C_2H_2 \rightarrow 2C(S) + H_2, \tag{R1}$$

$$C_2H_2 + nC(S) \rightarrow (n+2)C(S) + H_2, \tag{R2}$$

with the reaction rates given as

$$r_1 = k_1(T)[C_2H_2], \tag{13}$$

$$r_2 = k_2(T) f(A_s)[C_2H_2], \tag{14}$$

where $f(A_s)$ denotes the functional dependence on soot surface area per unit volume. In this paper, we simply assume that the functional dependence is linear, i.e. $f(A_s) = A_s$, which means that surface growth has a linear dependence on soot particle surface area.

The oxidation processes are very important for accurate predictions of soot in flames. The oxidation occurs primarily as a result of attack by molecular oxygen (O_2) and the OH radical. The radical O also contributes to soot oxidation in some regions [25]. We, therefore, account for the soot oxidation by O_2, OH and O, and assume the following reactions:

$$0.5O_2 + C(S) \rightarrow CO, \tag{R3}$$

$$OH + C(S) \rightarrow CO + H, \tag{R4}$$

$$O + C(S) \rightarrow CO. \tag{R5}$$

The reaction rates for these three reactions are obtained by

$$r_3 = k_3(T)T^{1/2}A_s[O_2], \tag{15}$$

$$r_4 = \varphi_{OH}k_4(T)T^{-1/2}A_sX_{OH}, \tag{16}$$

$$r_5 = \varphi_O k_5(T)T^{-1/2}A_sX_O, \tag{17}$$

where X_{OH} and X_O denote the mole fractions of OH and O, and φ_{OH} and φ_O are the collision efficiencies for OH and O attack on soot particles. The collision efficiency of OH is treated as that described by Kennedy *et al* [26], who accounted for the variation of the collision efficiency of OH with time by assuming a linear relation between the collision efficiency and a dimensionless distance from the fuel nozzle exit. A collision efficiency of 0.5 for radical O attack on the particles is used [27].

All the reaction rate constants, k_i $(i = 1, \ldots, 5)$, are given in table 1.

Table 1. Rate constants, as $A\exp(-E/RT)$ (units are kg, m, s, kcal, kmol and K).

k_i	A	E	Reference
k_1	1.35E + 06	41	[23]
k_2	5.00E + 02	24	[23]
k_3	1.78E + 04	39	[23]
k_4	1.06E + 02	0	[25]
k_5	5.54E + 01	0	[27]

The source term S_N in equation (10) accounts for the soot nucleation and agglomeration, and is calculated as

$$S_N = \frac{2}{C_{\min}} N_A R_1 - 2C_a \left(\frac{6M_{C(S)}}{\pi\rho_{C(S)}}\right)^{1/6} \left(\frac{6\kappa T}{\rho_{C(S)}}\right)^{1/2} [C(S)]^{1/6}[\rho N]^{11/6}, \quad (18)$$

where N_A is Avogadro's number (6.022×10^{26} particles kmol^{-1}), $C_{\min}$ is the number of carbon atoms in the incipient carbon particle (9×10^4), κ is the Boltzmann constant (1.38×10^{-23} J K^{-1}), $\rho_{C(S)}$ is the soot density (1800 kg m^{-3}) and C_a is the agglomeration rate constant for which a value of 3.0 [23] is used.

2.4. Numerical model

The governing equations are discretized using the control volume method. The SIMPLE numerical scheme [28] is used to deal with the pressure and velocity coupling. The diffusion and convective terms in the conservation equations are respectively discretized by the central and upwind difference methods. The discretized equations of gas species, soot mass fraction and soot number density are solved in a fully-coupled fashion on every grid to speed up the convergence process [29], while those of momentum, energy and pressure correction are solved using the TDMA method.

The computational meshes used in the two simulations are shown in figure 2. Totally 104×70 and 114×71 non-uniform grids are used for the two simulations, respectively. Finer grids are placed in the primary reaction zone and near the fuel nozzle inlet region. It has been

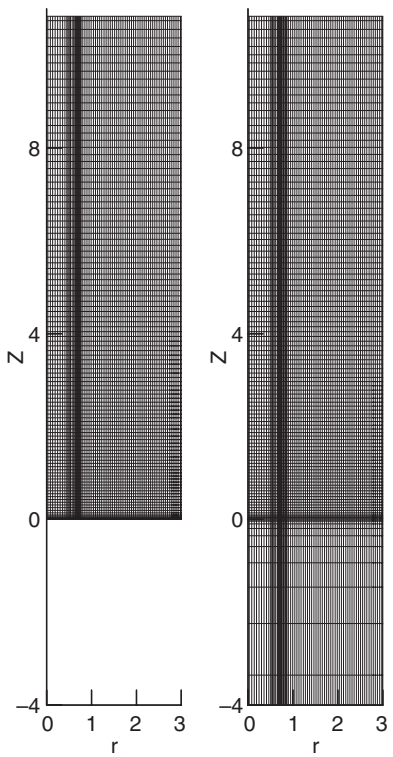

Figure 2. Computational meshes. Left: simulation 1; right: simulation 2.

checked that the further increase of grid number does not significantly influence the simulation results.

The chemical reaction mechanism used is essentially from GRI-Mech 3.0 [30], with the removal of all the reactions and species related to NO_X formation. The revised reaction scheme consists of 36 species and 219 reactions. All the thermal and transport properties are obtained by using the database of GRI-Mech 3.0 [30] and the algorithms given in [18, 31].

3. Results and discussions

3.1. Velocity and temperature profiles at the nozzle exit

Figure 3 illustrates the velocity and temperature profiles at the nozzle exit obtained by simulation 2. The velocity profile of simulation 1 at $z = 0$ (specified) is also shown for comparison. Since both fuel and air streams obtain energy from the fuel nozzle and flame base, their temperatures are higher than room temperature (300 K), and the velocity profiles are different from those of fully developed flows in a round pipe and a concentric space. The average temperatures of fuel and air streams at the nozzle exit from simulation 2 are respectively 131 and 29 K higher than room temperature. Therefore, applying the same temperature increase for both air and fuel streams to account for the preheating is not appropriate.

In the boundary layers next to the fuel nozzle, both fuel and air stream temperatures are significantly increased. Their values are even higher than the nozzle temperature at $z = 0$ (403 K). Therefore, both fuel and air streams obtain energy directly from the flame at $z = 0$. The temperatures of the air stream are higher than those of the fuel stream in the boundary layers, since the position of the flame base is located at the outside of the fuel nozzle (as we shall discuss below). However, due to the higher flow rate of the air stream compared to the fuel stream, the preheated region of the air stream is only limited to a narrow layer, while that of the fuel stream is extended to the centre of the fuel nozzle. Therefore, the predicted average temperature of the fuel stream is much higher than that of the air stream.

The velocity profile of the fuel stream obtained by simulation 2 at the nozzle exit is neither the general parabolic shape of a fully-developed flow in a round pipe nor a uniform distribution.

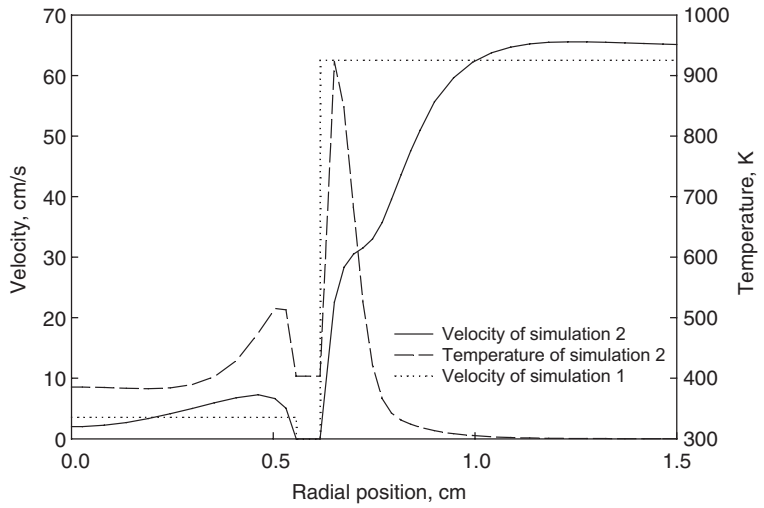

Figure 3. Predicted axial velocity and temperature profiles at $z = 0$ cm.

It gradually increases with increasing radius, except in the boundary layer next to the wall. The velocities of simulation 2 are higher than those of simulation 1 at $z = 0$, except in the centreline region and the narrow boundary layer next to the fuel nozzle. Apparently, these are due to the preheating. For the air stream, velocity increases quickly to a constant value with increasing radial distance from the outside of the fuel nozzle.

3.2. Velocity profiles above the nozzle exit

Figure 4 shows the radial velocity profiles along the axial direction at $r = 0.545$ which is the inner radius of the fuel nozzle. It illustrates that in simulation 1, air convects to the centreline region faster than in simulation 2 at lower axial heights. This is caused by the uniform velocity distribution of the air stream and the lower inlet fuel stream velocity in simulation 1. Although the velocity data are not available from the experiments of [8], the flame base positions (see the discussion in the next section) predicted by the two simulations show that this result is qualitatively reasonable. As a result, axial velocities of simulation 1 soon become higher than those of simulation 2 in the centreline region once z is greater than 0, as shown in figure 5, although axial velocities of the fuel stream of simulation 1 are lower than those of simulation 2 in most regions at $z = 0$. Figure 5 shows that axial velocities of simulation 2 are higher than those of simulation 1 in the centreline region once z becomes greater than 1 mm.

Since velocity affects the residence time, the differences of velocity profiles between two simulations may affect the flame temperature and soot predictions.

3.3. Flame temperatures

The flame temperatures predicted by the two simulations and those measured by Gülder *et al* [8], using CARS, are shown in figure 6. Figure 7 gives the radial temperature profiles at two axial heights. It can be seen that both simulations capture the general feature of the flame,

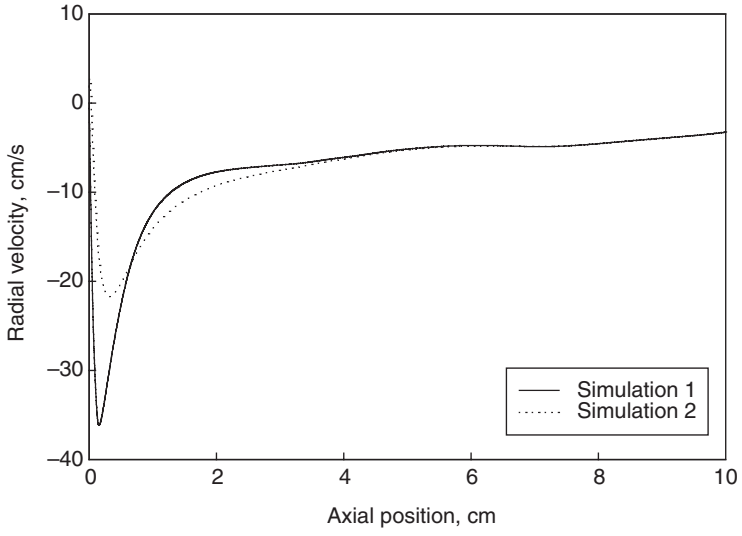

Figure 4. Radial velocity profiles along the axial direction at $r = 0.545$ cm.

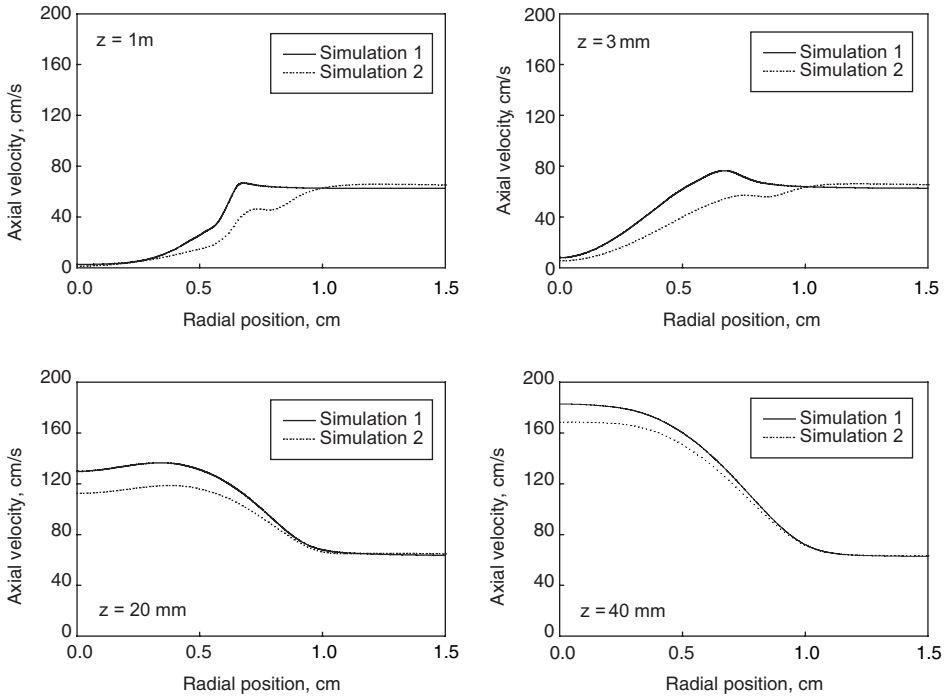

Figure 5. Axial velocity profiles at different axial heights.

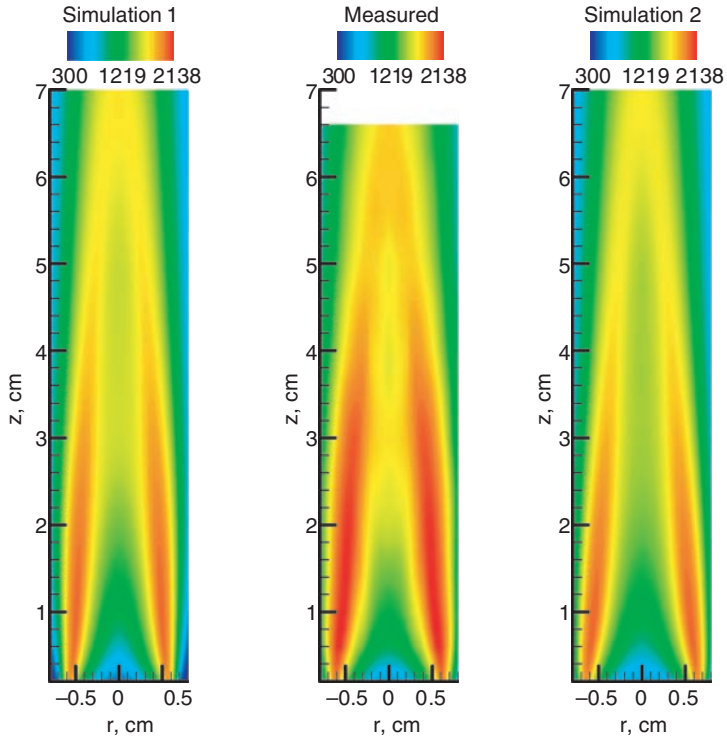

Figure 6. Flame temperatures (K).

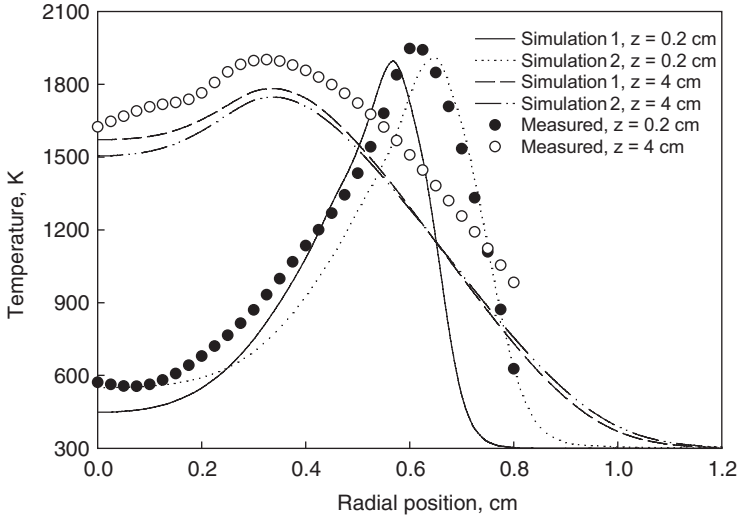

Figure 7. Radial temperature profiles at two axial heights.

i.e. the temperature profiles have a maximum in the annular region of the lower part of the flame, and these maximum temperature contours do not converge to the axis in the upper part of the flame. This is due to the radiation cooling by soot, since a significant amount of soot exists in the upper part of the flame (see the result below).

However, quantitatively simulation 2 (with the extended calculation domain) provides an improved result, especially for the lower part of the flame. First, the predicted temperatures by simulation 2 in the region immediately above the fuel nozzle are higher than those predicted by simulation 1. The temperature on the centreline at 2 mm height above the fuel nozzle exit is about 574 K, which is quite close to the value of 595 K from the experiment [8] at the same position, while simulation 1 gives a much lower value (477 K) at that location. Secondly, the radius of the flame base predicted by simulation 2 is closer to that obtained by the experiment, while simulation 1 underpredicts this value. This is the result of different velocity and temperature profiles at the nozzle exit in the two simulations. The higher temperatures at the nozzle exit increase the axial velocities of the fuel stream at $z = 0$ in simulation 2. The higher axial velocities of the fuel stream and the lower axial velocities of the air stream in the boundary layer next to the outside surface of the fuel nozzle for simulation 2 allow the fuel to move outwards along the radial direction, as shown by the radial velocity profiles at the lower axial positions in figure 4. Finally, we also observe that the annular region of higher temperatures predicted by simulation 2 is broader than that of simulation 1, although it is still narrower than the experiment. Since soot is usually formed in the lower part of the flame, we can expect that these differences may result in different soot volume fractions for the two simulations.

For the upper half of the flame, both simulations give similar temperatures, which are lower than the experimental result. This may be caused by the simplification of the soot model. As indicated by Sunderland and Faeth [32], soot nucleation is a complex process involving polycyclic aromatic hydrocarbons (PAH) that eventually become visible soot particles, although it can be empirically correlated with C_2H_2 concentration alone, as expressed by (R1). Moreover, not only C_2H_2 but also some other species may contribute to the soot surface growth process, which can be described by the effects of various species on active sites and parallel channels [32–34]. The simplifications in the current soot model need

to be improved in the future simulation to account for the complex soot inception and surface growth processes.

The peak flame temperature obtained by simulation 2 is only 7 K higher than that by simulation 1, since different soot volume fractions are obtained in the two simulations.

3.4. Soot volume fraction

Figures 8 and 9 depict soot volume fractions from the experiment [8] and the two simulations. Again, although both simulations capture the general features of soot in the flame, simulation 2 provides a more reasonable quantitative result. The peak soot volume fraction from simulation 2 (7.2 ppm) is higher than that (6.2 ppm) from simulation 1 and closer to that (8.0 ppm) from the experiment. Moreover, simulation 2 gives improved prediction in the centreline region.

The reason why simulation 2 provides a more reasonable result can be explained by the distributions of temperature and the mass fractions of acetylene from the two simulations. Figure 10 shows the mass fractions of acetylene predicted by the two simulations.

As discussed above, the temperatures in the lower centreline region are raised and the axial velocities there are lower in simulation 2. These cause the centreline fuel to decompose earlier in simulation 2. Meanwhile, since the flame base (the reaction zone in the lowest region) moves further away from the centreline in simulation 2, the fuel conversion region becomes wider. In figure 10, one can observe that acetylene is formed earlier in the centreline region, and the annular region with higher acetylene concentration is slightly wider in simulation 2.

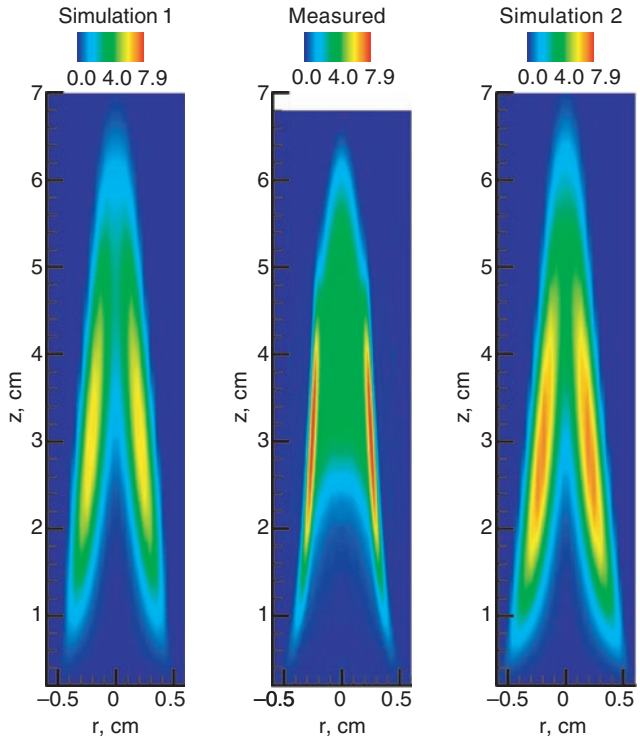

Figure 8. Soot volume fractions (ppm).

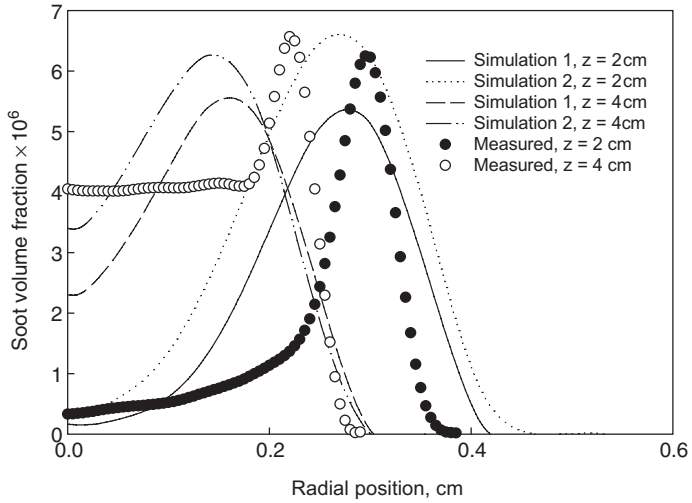

Figure 9. Radial soot volume fraction profiles at two axial heights.

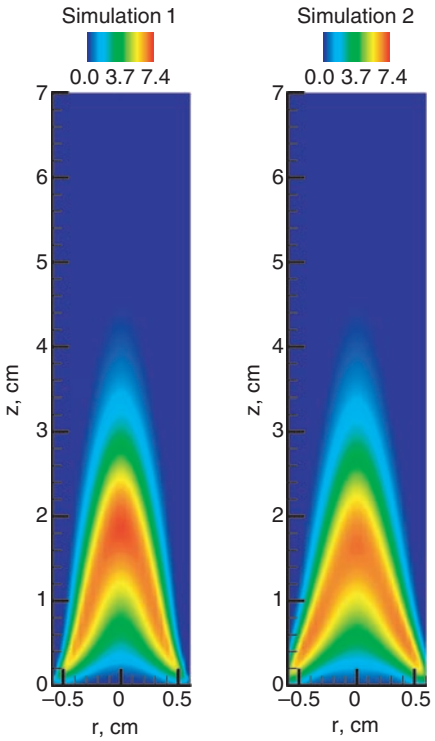

Figure 10. Predicted acetylene (C_2H_2) mass fraction distribution (%).

Consequently, soot inception and growth time increase in simulation 2, and therefore finally the soot yields increase.

We can therefore conclude that flame preheating results in a significant change in the prediction of soot yields.

4. Conclusions

An axisymmetric, laminar, coflow diffusion ethylene–air flame has been modelled by two different methods to deal with the inlet boundary conditions. The first method cannot accurately account for the influence of flame preheating, while the second one can.

The results show that the influence of flame preheating is important for the prediction of the soot formation process. Although both simulations capture the general feature of the flame, simulation 2 (which accounts for the influence of flame preheating) gives improved quantitative results compared to simulation 1. The peak soot volume fraction obtained by simulation 2 is about 1 ppm higher than that obtained by simulation 1 and is closer to the measured value. The soot volume fraction prediction of the centreline region is improved by simulation 2. The use of equal temperature increase for the fuel and air streams was found to be inappropriate. The velocity profiles of the fuel and air streams at the nozzle exit are neither the general profiles of fully developed flows in a round pipe and a concentric space nor uniform distributions.

References

[1] Smooke M D, Mitchell R E and Keys D E 1989 *Combust. Sci. Technol.* **67** 85–122
[2] Xu Y, Smooke M D, Lin P and Long M B 1993 *Combust. Sci. Technol.* **90** 289–313
[3] Bennett B A V and Smooke M D 1998 *Combust. Theory Modelling* **2** 221–58
[4] Zhang Z and Ezekoye O A 1998 *Combust. Sci. Technol.* **137** 323–46
[5] Smooke M D, Mcenally C S, Pfefferle L D, Hall R J and Colket M B 1999 *Combust. Flame* **117** 117–39
[6] McEnally C S, Schaffer A M, Long M B, Pfefferle L D, Smooke M D, Colket M B and Hall R J 1998 *27th Int. Symp. Combustion* (Pittsburgh, PA: The Combustion Institute) pp 1497–505
[7] Guo H, Liu F, Smallwood G J and Gülder Ö L 2001 *ASME Paper* NHTC2001-20126
[8] Gülder Ö L, Snelling D R and Sawchuk R A 1996 *26th Int. Symp. Combustion* (Pittsburgh, PA: The Combustion Institute) pp 2351–7
[9] Gülder Ö L, Thomson K A and Snelling D R 2000 *Proc. 2000 Spring Technical Meeting* (Ottawa: Combustion Institute/Canadian Section) pp 20.1–20.6
[10] Kuo K K 1986 *Principles of Combustion* (New York: Wiley)
[11] Chase M W, Davies C A, Downey J R, Frurlp D J, McDonald R A and Syverud A N 1985 *JANAF Thermochemical Tables* 3rd edn (New York: American Chemical Society and American Institute of Physics)
[12] Liu F, Smallwood G J and Gülder Ö L *AIAA Paper* 99-3679
[13] Liu F, Smallwood G J and Gülder Ö L 2000 *J. Thermophys. Heat Transfer* **14** 278–81
[14] Liu F, Smallwood G J and Gülder Ö L 2001 *J. Quant. Spectrosc. Radiat. Transfer* **68** 401–17
[15] Liu F, Smallwood G J and Gülder Ö L 2000 *Int. J. Heat Mass Transfer* **43** 3119–35
[16] Soufiani A and Taine J 1997 *Int. J. Heat Mass Transfer* **40** 987–91
[17] Dalzell W H and Sarofim A F 1969 *J. Heat Transfer* **91** 100–4
[18] Kee R J, Warnatz J and Miller J A *Sandia Report* SAND 83-8209
[19] Frenklach M, Clary D W, Gardiner W C and Stein S E 1984 *20th Int. Symp. Combustion* (Pittsburgh, PA: The Combustion Institute) pp 887–901
[20] Frenklach M and Wang H 1990 *23rd Int. Symp. Combustion* (Pittsburgh, PA: The Combustion Institute) pp 1559–66
[21] Frenklach M and Wang H 1994 *Soot Formation in Combustion: Mechanisms and Models* ed H Bockhorn *(Springer Series in Chemical Physics vol 59)* (Berlin: Springer) pp 162–90
[22] Leung K M, Lindstedt R P and Jones W P 1991 *Combust. Flame* **87** 289–305
[23] Fairweather M, Jones W P and Lindstedt R P 1992 *Combust. Flame* **89** 45–63
[24] Talbot L, Cheng R K, Schefer R W M and Willis D R 1980 *J. Fluid Mech.* **101** 737–58
[25] Neoh K G, Howard J B and Sarofim A F 1981 *Particulate Carbon: Formation During Combustion* ed D C Siegla and G W Smith (New York: Plenum) p 261
[26] Kennedy I M, Yam C, Rapp D C and Santoro R J 1996 *Combust. Flame* **107** 368–82
[27] Bradley D, Dixon-Lewis G, Habik S E and Mushi E M 1984 *20th Int. Symp. Combustion* (Pittsburgh, PA: The Combustion Institute) pp 931–40
[28] Patankar S V 1980 *Numerical Heat Transfer and Fluid Flow* (New York: Hemisphere)
[29] Liu Z, Liao C, Liu C and McCormick S *AIAA Paper* 95-0205

[30] Smith G P, Golden D M, Frenklach M, Moriarty N W, Eiteneer B, Goldenberg M, Bowman C T, Hanson R K, Song S, Gardiner W C Jr, Lissianski V V and Qin Z http://www.me.berkeley.edu/gri_mech/
[31] Kee R J, Miller J A and Jefferson T H *Sandia Report* SAND 80-8003
[32] Sunderland P B and Faeth G M 1996 *Combust. Flame* **105** 132–46
[33] Mauss F, Schafer T and Bockhorn H 1994 *Combust. Flame* **99** 697–705
[34] Kennedy I M 1997 *Prog. Energy Combust. Sci.* **23** 95–132